DCE-MRI Breast Image Segmentation Using Modified VGG-16 Network with Image Enhancement Based on Bounded Turning Mittag-Leffler Function

Ali Shamkhi[1,*], Hadeel Aljobouri[1] and Ali Hasan[2]

[1]Affiliation 1 (Department of Biomedical Engineering/College of Engineering, Al-Nahrain University), Baghdad, Iraq
[2]Affiliation 2, (Department of Physiology and Medical Physics/College of Medicine, Al-Nahrain University), Baghdad, Iraq

[*]Corresponding Author: Ali Shamkhi. Email: aali.ibrahim.phd2023@ced.nahrainuniv.edu.iq

ABSTRACT: Accurate lesion segmentation is a critical component of computer-aided diagnosis for breast cancer, as it enables precise lesion delineation and robust quantitative assessment. However, breast lesion segmentation remains challenging because of tumor heterogeneity, variations in fibroglandular tissue, and the complex morphology of breast lesions. Dynamic contrast-enhanced magnetic resonance imaging (DCE-MRI) has emerged as an effective modality for the early detection and characterization of breast lesions due to its ability to capture detailed information on tumor morphology and microenvironment. This study proposes a two-stage framework for breast DCE-MRI lesion segmentation. In the first stage, bounded turning Mittag-Leffler enhancement is applied to improve image quality and enhance lesion-relevant structures. In the second stage, an extended Visual Geometry Group (VGG)-based network with dilated convolution is employed to segment breast lesions. The proposed framework was evaluated on a public multicenter dataset comprising 979 pre-treatment T1-weighted cases and 10,863 bitmap slice images converted from original Neuroimaging Informatics Technology Initiative (NIFTI) volumes with expert voxel-level annotations. The dataset was divided into training, validation, and testing subsets at ratios of 68%, 12%, and 20%, respectively. Based on 5-fold cross-validation, the proposed method achieved an accuracy of 98.73%, a Dice coefficient of 91.56%, and a Jaccard index of 85.41%. Furthermore, the framework demonstrated competitive performance compared with related studies. These findings confirm the effectiveness of the proposed framework for breast DCE-MRI lesion segmentation and highlight its potential to improve the accuracy and reliability of breast cancer computer-aided diagnosis systems.

KEYWORDS: Breast cancer; Lesion segmentation; DCE-MRI; Mittag-Leffler enhancement; Deep learning; VGG-based

1 Introduction

Computer-aided diagnosis (CAD) systems are becoming more significant in the area of breast cancer diagnosis since it enhances the uniformity, effectiveness, and repeatability of radiology interpretation. This value can be especially seen in the area of DCE-MRI, where lesion characterization is determined solely by the morphological appearance and contrast-enhancement in relation to kinetics [1,2]. A common breast DCE-MRI CAD scheme has four key steps: the image series acquired is processed, the region of interest (ROI) known to contain suspicious enhancement is identified, quantitative descriptors are extracted at the ROI, and classification/segmentation

algorithms are applied to produce the ultimate diagnostic result [3]. Lesion segmentation is one of such stages, since precise segmentation has a direct impact on subsequent analysis of shapes, textures, and kinetic features, malignancy, treatment planning, and assessment of therapy response [2].

Despite its clinical significance, automated segmentation of breast lesions in DCE-MRI remains a challenging task. This difficulty is mainly attributed to heterogeneous tumor enhancement, variations in fibroglandular tissue, complex lesion morphology, partial-volume effects, and motion artifacts between dynamic phases. In addition, background parenchymal enhancement can obscure lesion margins or mimic abnormal enhancement, making the separation of tumor tissue from surrounding normal tissue particularly difficult when based primarily on intensity information [4–6]. Because segmentation accuracy is strongly dependent on lesion conspicuity and boundary visibility, image enhancement is often employed as a preprocessing step to improve local contrast, suppress noise, and sharpen lesion edges before ROI localization and pixel-wise prediction[7]. In this regard, fractional-calculus-based operators are of particular interest because they offer flexible control between smoothing and sharpening through fractional-order modeling, enabling subtle tissue transitions to be enhanced adaptively. Within this context, Mittag-Leffler-based formulations have emerged as promising tunable filtering approaches in medical image analysis, with potential benefits for improving lesion detection and segmentation especially DCE-MRI [8,9].

Recent advances in deep learning have substantially improved medical image segmentation and have demonstrated that automated delineation can be much faster than manual annotation while maintaining clinically useful agreement [10]. Encoder-decoder architectures, especially U-Net and its variants, have become dominant in biomedical segmentation because they combine hierarchical feature learning with multiscale context aggregation and skip connections for precise boundary localization [11]. Transfer learning has further strengthened this field, with pretrained backbones such as VGG-16 being adapted to dense prediction tasks to compensate for limited annotated breast DCE-MRI datasets and to accelerate convergence [8,12]. Several recent studies have reported promising results for breast DCE-MRI segmentation. Feng et al. enhanced active contour segmentation using extreme learning machine priors and fuzzy C-means clustering, achieving a Dice score of 0.858 and a Jaccard index of 0.757 [13]. Khaled et al. proposed a U-Net ensemble trained on different DCE inputs and reported a mean Dice score of 0.680 overall and 0.802 for main lesions [14]. Douglas et al. compared 2D quasi-3D U-Nets with full 3D U-Nets with first- and second-postcontrast subtraction images of 994 distinct lesions (mass and non-mass lesions). The quasi-3D U-Net using second-postcontrast images delivered median Dice scores of 0.806 and 0.699 using mass and non-mass lesions, respectively, with a median Hausdorff of 6.88 mm and 11.05 mm respectively. At that, their results indicated that the quasi-3D U-Net was superior in the combination of Dice similarity compared to the full 3D U-Net and also needed less computational cost [15]. Hizukuri et al. applied ResUNet++ with slice-sequence learning and cross-phase convolution for non-mass enhancement segmentation, achieving a Dice score of 0.712, Jaccard 0.563, and sensitivity 0.727 [16]. More recently, Star et al. integrated modified ResNet50 backbones into DeepLabV3+ and obtained a Dice score of 0.92 [17], while Garrucho et al. introduced the large multicenter MAMA-MIA dataset and established strong nnU-Net segmentation baselines. Their baseline vanilla nnU-Net, trained on the full dataset, achieved a mean validation Dice score of 0.7620 ± 0.2113, providing a strong segmentation benchmark

for future studies [18]. Collectively, these studies confirm the potential of convolutional neural networks for breast DCE-MRI segmentation, while also indicating the continued need for robust preprocessing and multiscale feature modeling to address low-contrast margins and complex enhancement patterns [14,19,20]

To address these challenges, this study proposes a two-stage pipeline for breast cancer lesion segmentation in DCE-MRI. In the first stage, a bounded-turning Mittag-Leffler (BT-ML) enhancement approach is applied as a preprocessing step to improve lesion conspicuity, sharpen lesion-parenchyma boundaries, and enhance phase-dependent contrast without excessively amplifying already bright regions [5,21,22]. In the second stage, a transfer-learning-based segmentation framework is developed using a VGG-16 encoder initialized on ImageNet and fine-tuned on breast DCE-MRI data. To improve multiscale representation of both mass and non-mass enhancement patterns, dilated convolutions are incorporated into the VGG-based architecture, enlarging the receptive field while preserving spatial resolution [23,24]. By combining intensity-aware enhancement with a deep segmentation network, the proposed framework is designed to provide more stable and accurate lesion delineation in the presence of background parenchymal enhancement and low-contrast tumor margins, thereby improving segmentation performance and reducing the burden of manual correction in breast cancer imaging workflows [25].

2 Materials and Methods

The proposed study comprises two stages: the preprocessing of DCE-MRI images and VGG-16-based segmentation of the infected breast region.

2.1 Dataset

The suggested approach was assessed on a public multicenter breast DCE-MRI dataset comprising 979 pre-treatment T1-weighted cases and 10,863 BMP slice images generated from original NIfTI volumes. The dataset was assembled from The Cancer Imaging Archive (TCIA) collections, including I-SPY2 and ACRIN 6698, and included expert voxel-level annotations of primary tumors and non-mass enhancement verified by 16 breast imaging specialists [26]. Each case included expert voxel-level tumor annotations. The dataset comprised axial acquisitions with standardized orientation and phase naming, and no global preprocessing was applied to preserve native resolution. All imaging volumes and annotations are publicly available through the CC BY-NC license for the MAMA-MIA Synapse repository [27]. For model development, the dataset was split into training, validation, and testing sets of 7.387 (68%), 1.303 (12%), and 2.173 (20%) images, respectively.

2.2 Preprocessing

Noise and motion artifacts, inhomogeneity of intensity between coils, and phase-to-phase differences of contrast usually appear in breast DCE-MRI images. These artifacts both deteriorate image quality and add slice and phase-dependent intensity drifts, as well as can blur or otherwise distort lesion boundary delineation, increasing challenges of reliably separating normal parenchyma, pectoral muscle, and tumor (mass and non-mass enhancement). Pre-processing applies mitigation to the effects to enhance the fidelity of subsequent analysis, either automatically

done by learning algorithms or by radiologists. Common processes are breast masking, inter-phase motion correction (phase to a reference phase), optional bias -field correction, intensity standardization per phase, denoising preserving edge information, and generation of subtraction images to bring out contrast kinetics. One of the main aims of this step is proper segmentation, i.e., the isolation of the lesion from the surrounding tissues such that the results of the next action in regard to measurements and classifications are sound. To strengthen boundary definition and reduce inter- and intra-exam variability before segmentation, the pipeline employs an image enhancement operator based on the bounded-turning Mittag-Leffler (BT-ML) function. Within the framework of complex differential equations, bounded-turning functions serve as controlled, edge-aware transforms [28]. In this context, a BT-ML operator enhances lesions to background contrast in each DCE phase while limiting over-sharpening and artifact amplification, as shown in Fig. 1. Applying BT-ML consistently across phases yields inputs with more uniform intensity behavior and crisper lesion contours, decreasing the likelihood of pixel-level misclassification by the subsequent VGG-16-based segmentation model and improving multi-phase delineation of both mass and non-mass enhancement. In this work, all breast DCE-MRI phases are enhanced using a BT-ML operator as a new preprocessing method to reduce intra- and inter-phase variability and sharpen lesion margins. All breast DCE-MRI slices were processed using the proposed BT-ML enhancement to suppress variability within and across scans [28]. Complex differential equations (CDEs) underpin numerous image-processing operations and are especially powerful for enhancement procedures. Within the framework of complex differential equations, bounded-turning functions are complex-valued mappings that restrict the angular change they introduce. A standard illustration is a pure rotation: multiplying any complex number by the imaginary unit maps it to a new complex number whose modulus is unchanged. Meanwhile, it turns 90 degrees in the direction counterclockwise. Since rotation is regulated in such a way that no magnitude is modified, bounded-turning functions come in handy in image processing to highlight edges and boundaries, but not to enhance artifacts [29]. Within this paper, it is proposed that a generalized bounded-turning transform using the Mittag-Leffler function will be used in order to increase contrast at lesion boundaries and reduce inter and intra-phase changes before segmentation. The bounded-turning Mittag-Leffler function is a variant of the classical Mittag-Leffler function based on formal classifications of fractional calculus kernels and useful in the modeling and solution of fractional- order dynamics. In comparison with the normal form of solution operators of discrete-time fractional differential equations, the bounded-turning formulation extends the structure but imposes bounded variation of the complex argument in ensuring controlled angular action [30]. It produces a versatile, mathematically based operator with extensive application both in science and engineering, and it provides a more generic functional foundation compared to standard kernels to design and stabilize the construction of image enhancement based on fractional differential equations. We use a generalized bounded-turning transform based on one parameter of the Mittag-Leffler function, which is evaluated at a fictitious argument, in this work, to control the angular change, but retain the magnitude in the complex plane [29,30]. The convergent series is a definition of the one-parameter Mittag-Leffler function.

$$E_a(w) = \sum_{k=0}^{\infty} \frac{w^k}{\Gamma(1+ak)}, \quad a > 0 \tag{1}$$

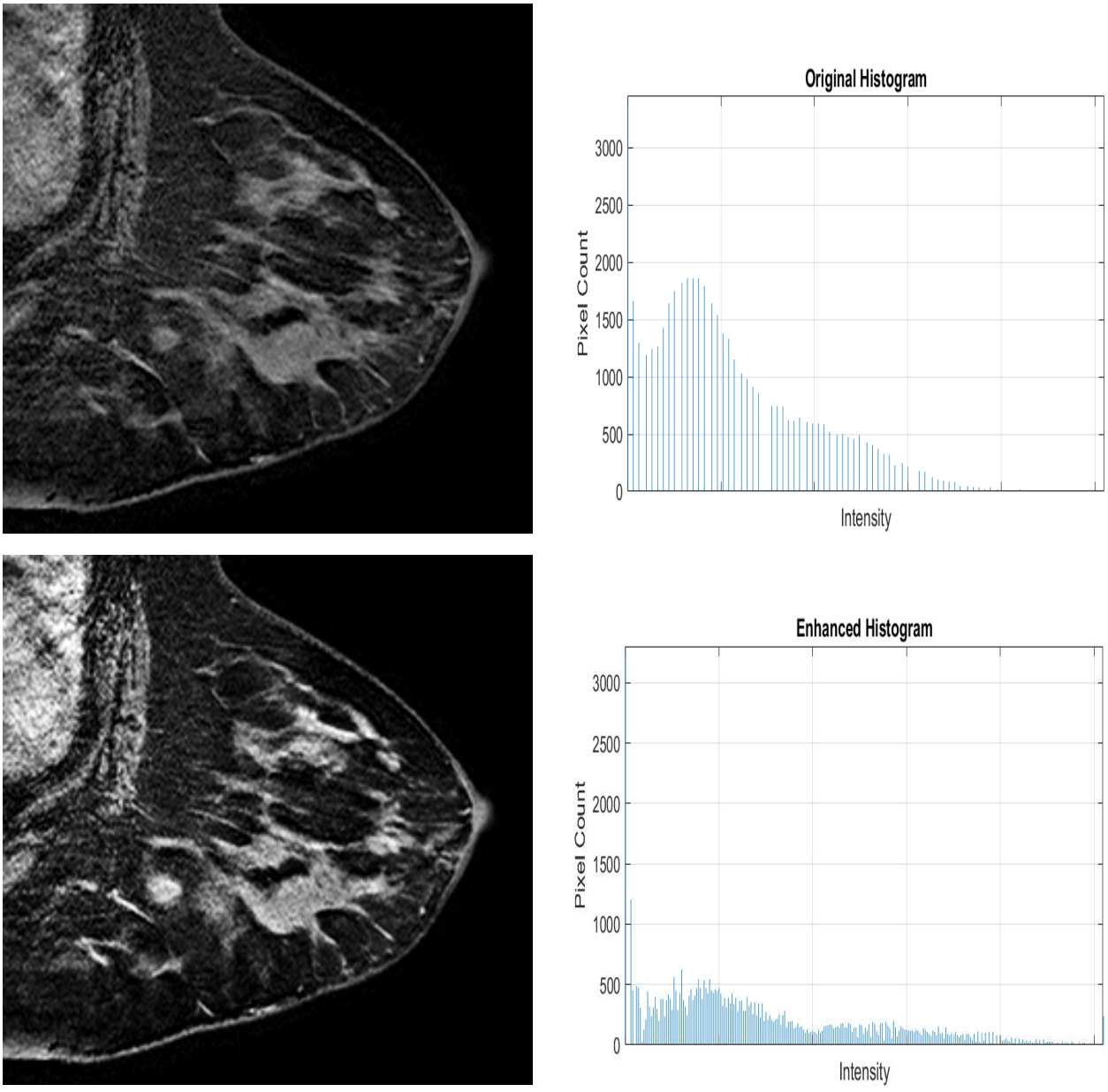

Figure 1: Histogram results, original input, and enhanced images: (a) original image, (b) original histogram, (c) processed image, and (d) histogram result.

Accordingly, for an imaginary argument w=iz, its series expansion becomes:

$$E_a(iz) = 1 + \frac{iz}{\Gamma(1+a)} - \frac{z^2}{\Gamma(1+2a)} - \frac{iz^3}{\Gamma(1+3a)} + \frac{z^4}{\Gamma(1+4a)} + \frac{iz^5}{\Gamma(1+5a)} - \frac{z^6}{\Gamma(1+6a)} \tag{2}$$

For the bounded-turning Mittag-Leffler function $E_a(iz)$, with fractional order $a > 0$, the series coefficients satisfy uniform bounds in the open unit disk, where $|z| = r < 1$ and r denotes the pixel probability. Specifically:

$$t_0 = 1, \quad |t_1| \leq \frac{r}{\Gamma(1+a)}, \quad |t_2| \leq \frac{r}{\Gamma(1+2a)}, \quad \ldots, \quad |t_n| \leq \frac{r}{\Gamma(1+na)} \tag{3}$$

These bounds follow directly from the power-series expansion in Equation 2. The first term yields $t_0 = 1$. For the next term:

$$t_1 = \frac{iz}{\Gamma(1+a)} \;\Rightarrow\; |t_1| \leq \frac{|iz|}{\Gamma(1+a)} \leq \frac{r}{\Gamma(1+a)} \tag{4}$$

Similarly,

$$t_2 = \frac{-z^2}{\Gamma(1+2a)} \;\Rightarrow\; |t_2| \leq \frac{|-z^2|}{\Gamma(1+2a)} = \frac{|z|^2}{\Gamma(1+2a)} = \frac{r^2}{\Gamma(1+2a)} \leq \frac{r}{\Gamma(1+2a)} \tag{5}$$

In general:

$$|t_n| \leq \frac{r^n}{\Gamma(1+na)} \leq \frac{r}{\Gamma(1+na)}, \qquad 0 < r < 1 \tag{6}$$

The corresponding image-domain operator can be written as:

$$T_{n,m}(i,j) = \sum_{i=0}^{n} \sum_{j=0}^{m} \left(G(i,j) \times \frac{r}{\Gamma(1+na)} \right) \tag{7}$$

here G(i,j) denotes the input image. An empirically chosen value, a = 0.75, produced the most favorable enhancement. The objective of the enhancement stage is to improve visual quality and clarity. Qualitatively, the post-processing images exhibit brighter, more distinct structures, with histogram analysis confirming distributional changes relative to the originals.

2.3 The Proposed Segmentation Approach

Transfer learning is adopted in this study to exploit the pretrained knowledge of the VGG-16 and adapt it to a related segmentation problem using a different dataset. The VGG-16 backbone is made up of the following five stages of a stack of thirteen convolutional layers. The first two convolutional layers, conv1-1 and conv1-2, have 64 kernel filters and operate at a spatial dimension of 224 x 224. The second two convolutional layers, conv2-1 and conv2-2, use 128 kernel filters and operate at (128×128). Convolutional layers number three (conv3-1, conv3-2, and conv3-3) operate at (64×64) with 256 kernel filters. Convolutional layers number four (conv4-1, conv4-2, and conv4-3) operate at (32×32) with 512 kernel filters. Conv5-1, Conv5-2, and Conv5-3 are the

fifth three convolutional layers that operate at (16×16) with 512 kernel filters. For all convolutional layers, the kernel size is (3×3), and the stride is fixed to one pixel. Finally, three fully connected layers follow the convolutional blocks in the original network, and the last layer is the SoftMax layer; the complete VGG-16 configuration is illustrated in Fig. 2. Since the original VGG-16 was developed for image classification, it must be customized for dense prediction. The periodic max-pooling operations in VGG-16 reduce the spatial size by a factor of 32 across the encoder until reaching the classification head, as illustrated in Fig. 2. To enable segmentation, the last three fully connected layers are replaced by three convolutional layers (Conv6-1, Conv6-2, and Conv6-3) of size (7×7) with 512 kernel filters, producing coarse confidence maps. Finer predictions are obtained by combining deep semantic features with shallower spatial features. Specifically, two (1×1) convolutional layers (Conv7 and Conv8) are applied to the outputs of Pool3 and Pool4 for dimensionality reduction, so that these feature maps can be summed with the outputs of two transposed-convolution layers (ConvTrans7 and ConvTrans8) with an up-sampling factor of (2×2), yielding higher-resolution intermediate predictions of (32×32×512) and (64×64×256), respectively. Finally, an additional transposed-convolution layer (ConvTrans9) with an up-sampling factor of (4×4) restores the prediction to the original breast DCE-MRI spatial size of (256×256×64). A terminal per-pixel class probability estimate is then produced by the SoftMax layer for the target breast DCE-MRI labels, completing the proposed network.

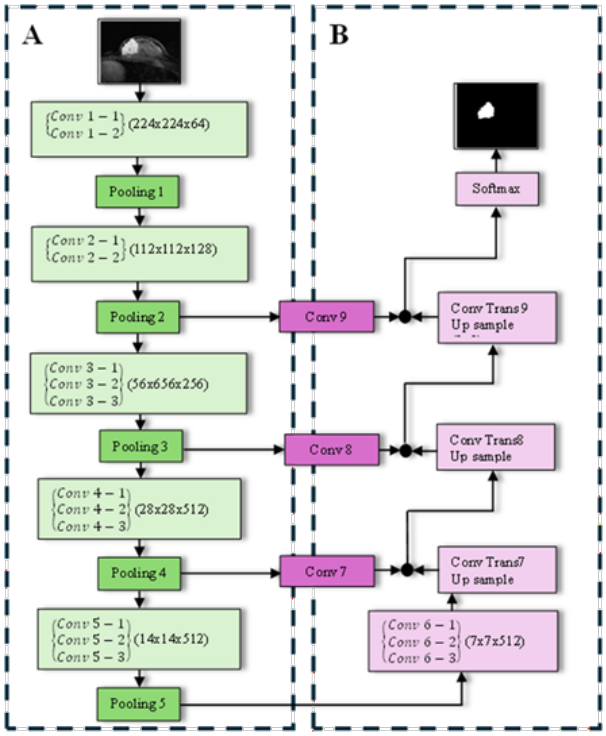

Figure 2: The proposed segmentation model.

2.4 Evaluation Metrics

The segmentation performance of the proposed breast DCE-MRI framework was assessed using accuracy (ACC), Dice similarity coefficient (DSC), and Jaccard coefficient (JC), which are standard metrics for quantifying agreement between predicted masks and reference annotations

in medical image segmentation. In this regard, the true positives (TP) represent lesion pixels that are correctly detected and labeled as lesion, the false positives (FP) are non-lesion pixels that were mistakenly identified and labeled as lesion, the true negatives (TN) are correctly identified background or normal tissue pixels, and the false negatives (FN) are those lesion pixels missed by the model. The accuracy (less key) is the total percentage of correct pixels; to prevent ACC performance in breast lesion segmentation is often strongly imbalanced (non-lesion tissue that dominates the image), and this should be used with care. In direct comparison, DSC and JC explicitly measure spatial overlap between ground-truth lesions and predicted ones, so this makes it more informative for small, irregular, or heterogeneous tumors. DSC (overlap-based, F1-like) is a balance between sensitivity and precision, and JC (also known as intersection over union) is more strict than DSC as an overlap criterion, and it is usually used along with DSC to indicate a more complete picture of segmentation accuracy, especially at the borders of lesions [31,32]. The metrics in his formal definitions are stated as:

$$ACC = \frac{TP + TN}{TP + TN + FP + FN} \tag{8}$$

$$DSC = \frac{2TP}{2TP + FP + FN} \tag{9}$$

$$JC = \frac{TP}{TP + FP + FN} \tag{10}$$

The DCE-MRI breast images often show significant noise and low-contrast tumor boundaries, which can hide important features. Such quality issues can make downstream analysis more difficult in medical imaging. Therefore, a preprocessing step was implemented to reduce noise and enhance critical structures. Generally, image preprocessing aims to improve image quality by reducing noise and artifacts while highlighting features like tumor margins. This step is crucial to ensure that the segmentation model can accurately interpret the data.

3 Results

The dataset's DCE-MRI scans have been divided into training (68%), validation (12%), and testing (20%) phases. The DCE-MRI dataset is split into five subgroups in order to apply five-fold cross-validation. The Intel Core i7-9750H 64-bit Windows 11 computer with 16GB RAM and an NVIDIA RTX 2070 GPU was used to build the scripts in Matlab 2024a.

The suggested network's processing time can be decreased by using bilinear interpolation to reduce the size of the training image. To lessen overfitting and enhance the network's generalization, different versions of each initial training DCE-MRI scan were produced using a variety of augmentation techniques, such as scaling, rotation, and reflection. The range of rotations was picked randomly for each image by rotating the image within a specified interval between -20° and 20° without resizing. Part A Fig. 2 of the proposed network was initialized with the original weights from VGG-16, which has been trained on millions of images. The weights of part B Fig. 2 were randomly initialized using the Xavier algorithm with biases set to zero initially. In

order to avoid neurons becoming stuck in saturation during training, the Xavier method is utilized to initialize the network's weights with more intelligent values. To minimize the mistakes of the suggested network and generate significantly better weights, the conventional stochastic gradient descent (SGD) based optimization approach is typically employed. Following successful training, the test DCE-MRI scans were fed into the suggested trained network for segmentation evaluation, along with the manual segmentation result as the gold standard. Figure 3, where the total number of successfully segmented pixels is calculated by comparing the anticipated output of the suggested network with the corresponding ground truth image. The limits of the lesion region detected by the suggested network are indicated in yellow, while the supplied ground truth annotations are indicated in red.

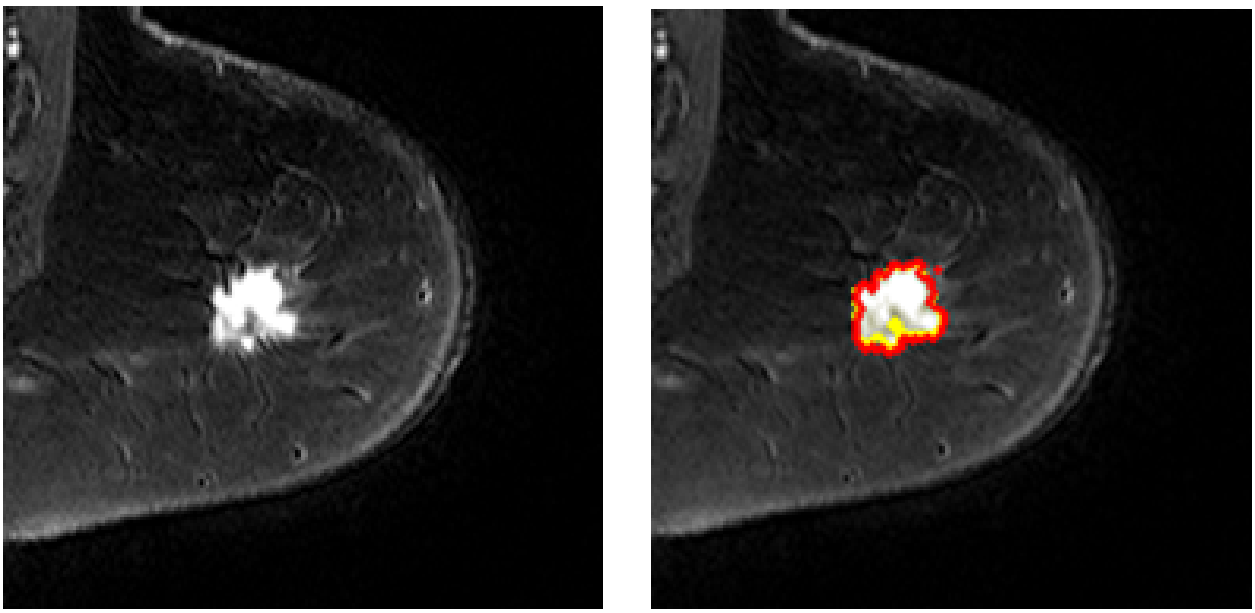

Figure 3: Qualitative comparison of segmentation results, where the ground truth mask is displayed in red and the segmented (predicted) mask is displayed in yellow.

As previously said, the segmentation for all 2173 DCE-MRI images for 5-fold cross-validation is assessed using three measures (ACC, DSC, and JC), as shown in Fig. 4. These measures are then averaged to get the average coefficient scores, which are summarized in Table **??**.

Table 1: Statistical performance of the proposed segmentation framework.

Metric	Mean	SD	Min	Max
Accuracy	0.9873	0.0022	0.9851	0.9895
Dice	0.9156	0.0118	0.9038	0.9274
Jaccard (IoU)	0.8541	0.0177	0.8364	0.8718

The proposed network was successfully applied to the downloaded breast DCE-MRI dataset. The ACC, DSC, and JC achieved were 98.73%±0.22, 91.56%±1.18, and 85.41%±1.77, respectively. The Dice coefficient results demonstrate the precision of the segmentation process, where the predicted segmentation is compared against the ground truth to quantify the degree of overlap and similarity between them.

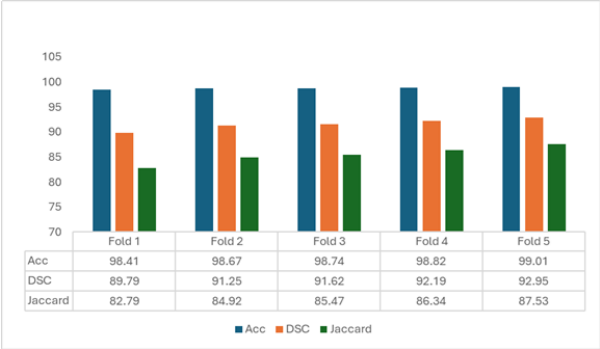

	Fold 1	Fold 2	Fold 3	Fold 4	Fold 5
Acc	98.41	98.67	98.74	98.82	99.01
DSC	89.79	91.25	91.62	92.19	92.95
Jaccard	82.79	84.92	85.47	86.34	87.53

Figure 4: Performance of the proposed framework across the 5 cross-validation folds in terms of Accuracy, Dice, and Jaccard.

4 Discussion

Variations in breast lesion enhancement patterns across different clinical stages, together with the effect of slice thickness during DCE-MRI acquisition, were among the primary challenges encountered during segmentation of the exported 2D BMP slices; therefore, acquiring images with thinner slices is important for improving boundary delineation and overall segmentation performance. In addition, early-stage lesions may show subtle contrast uptake and poorly defined margins, which increases boundary uncertainty and can lead to higher variability in the segmented lesion area on individual 2D slices, compared with lesions observed at later stages. To further validate the effectiveness of segmenting breast lesions in DCE-MRI, as shown in Table **??** the effectiveness of the suggested segmentation method was contrasted with several breast lesion segmentation strategies.

Table 2: Results of the proposed segmentation model and other segmentation techniques.

Reference	Approach	Accuracy (%)	Dice (%)	Jaccard (%)
Feng et al. (2022) [13]	3TP U-Net	99.98	61.24	–
Khaled et al. (2022) [14]	U-Net Ensemble (3D patch-based)	–	68.0	–
Douglas et al. (2023) [15]	AJPN (Attention-guided Joint-Phase-Learning Network)	–	86.0	75.0
Hizukuri et al. (2024) [16]	Phase-preserved denoising + adaptive Wiener filtering + CMF/min-cut	98.73	91.58	85.25
Star et al. (2025) [17]	DeepLabV3+ with modified ResNet50 backbones	–	92.0	–
Garrucho et al. (2025) [18]	Active Contour Model (ACM) using ELM + FCM	–	85.88	75.72
Proposed Model	**Modified Transfer Learning (VGG-16)**	**98.7**	**91.5**	**85.4**

As can be seen from the comparative results, the proposed breast DCE-MRI lesion segmentation framework achieved strong and stable performance, with Accuracy = 98.73% ± 0.22, Dice = 91.56% ± 1.18, and Jaccard = 85.41% ± 1.77. These results indicate a high degree of agreement between the predicted lesion regions and the reference annotations, while the low standard deviations suggest that the model maintained consistent performance across the evaluation folds. In particular, the Dice and Jaccard values confirm that the proposed framework achieved reliable lesion overlap rather than merely benefiting from the large proportion of background pixels [32]. Compared with previous studies, the proposed model outperformed several commonly reported breast DCE-MRI segmentation approaches. For instance, Feng et al. (2022) reported Accuracy = 99.98% ± 0.02 but only Dice = 61.24% ± 11.84 using 3TP U-Net [13]. Their accuracy level is alleged to be exceedingly high, yet such a result is probably due to the bias in the classes, where the background pixels take over the picture and artificially amplify the accuracy in spite of low overlap between lesions and masks. The proposed model, on the other hand, was much better at Dice, and this result suggests that it delineated the lesion regions more accurately. A comparable pattern can be made with references to Khaled et al. (2022), where the 3D patch-based U-Net ensemble obtained a mean Dice of 68.0%. [14], which is significantly smaller than the one reached by the proposed system. The proposed method was also found to be high in terms of the ability to overlap with the performances of other recent methods. According to Douglas et al. (2023), Dice = 86.0% and Jaccard = 75.0% of the attention-guided joint-phase-learning network (AJPN) [15]. They are also lower than the suggested metrics of overlap. Similarly, Dice = 85.88% ±6.62 and Jaccard = 75.72% ±9.68 were obtained with the active contour model reported by Garrucho et al. (2025) [18]. Overall, in both scenarios, the proposed framework had larger overlap metrics, and results imply that the combination between limited turning Mittag-Leffler enhancement and the modified transfer-learning VGG-16 architecture is more useful in representing lesion margins and enhancing the quality of segmentation in breast DCE-MRI. A more similar comparison is made with Hizukuri et al. (2024), who obtained Accuracy = 98.73%, Dice = 91.58%, and Jaccard = 85.25% through the use of a framework that is grounded on phase-preserved denoising, adaptive Wiener filtering, and CMF/min-cut segmentation [16]. Their Dice score is slightly higher than that of the proposed model by only 0.02 percentage points and the proposed framework had a slightly higher Jaccard score. This implies that both procedures are very similar in terms of the level of segmentation, although they are based on other principles of methodology. Nonetheless, the proposed solution has the merit of incorporating the image enhancement and deep transfer learning into a coherent learning-based framework, which can provide more flexibility to subsequent optimization and expansion. Also, it should be noted that the proposed model showed a Dice score of 92.0% with DeepLabV3+ with modified ResNet50 backbones [13], thereby falling a bit short of 91.56% reported by Star et al. (2025) using the same algorithm [17]. This not only facilitates the possibility that the innovative encoder-decoder frameworks with more updated features and robust multiscale feature extraction could still deliver the minor boost in pure Dice functionality. However, the distinction is not that broad, and the offered framework is very competitive, not to mention it also got high Jaccard and accuracy measures. Thus, the findings show that the modified transfer-learning VGG-16 model is an effective framework to use as a strong segmentation model to conduct breast DCE-MRI. All in all, these comparisons indicate that the proposed approach has good performance in comparison to a number of published breast DCE-MRI lesion segmentation systems and is tightly around the

best reported overlap scores of the selected literature. The results indicate that limited turning Mittag-Leffler enhancement, together with a modified VGG-16 network with transfer learning, was helpful to enhance the representation of lesions and exact boundary delineation. Simultaneously, the similarity of results of other recent techniques suggests that the breast DCE-MRI segmentation is still a difficult issue, and further enhancement could be provided by more effective backbone design, bigger multicentral datasets, and more effective utilization of multi-phase information.

5 Conclusion

One of the important CAD of the breast DCE-MRI is lesion segmentation because the accurate separation of tumors and fibroglandular tissue, as well as the separation of the tumor and background enhancement, is the key to the successful quantitative analysis. The proposed work presents a modified VGG-16 framework that is designed to work with 2D BMP slices of 3D DCE-MRI volumes. The image processing model (Mittag-Leffler-based) is very distinctive to the framework, as it enhances the conspicuity of lesions by suppressing unwanted pixels. Moreover, expansion of the receptive field can be achieved by additions of the dilated convolutions to enable the network to have an expanded ability to identify large contextual detail without compromising on the high-resolution edge details. The model with the Jaccard Index of 85.41% ±0.0177 and the Mean Dice Score of 91.5% ±0.0118 is much better aligned to expert ground truth. These results make the network a solid framework of application in downstream clinical applications, such as radiomics and diagnostic decision support.

Acknowledgement: The authors would wish to show their hearted thanksgiving to the editors and anonymous reviewers, they critically reviewed, gave very insightful suggestions and valuable comments, without which this manuscript would have been of very low quality.

Funding Statement: This research received no external funding and was fully funded by the authors.

Author Contributions:
Conceptualization, Hadeel Aljobouri and Ali Hasan; Methodology, Ali Hasan Ali Shamkhi; software,Ali Hasn and Ali Shamkhi; validation, Ali Hasan, Hadeel Aljobouri and Ali Shamkhi; formal analysis, Hadeel Aljobouri and Ali Hasan; investigation, Ali Hasan and Ali Shamkhi; data curation, Ali Shamkhi; writing—original draft preparation, Ali Shamkhi; writing—review and editing, Hadeel Aljobouri; visualization, Ali Shamkhi; supervision, Ali Hasan and Hadeel Aljobouri. All authors reviewed the results and approved the final version of the manuscript.

Availability of Data and Materials: The data supporting the findings of this study are openly available in the MAMA-MIA Synapse repository at https://www.synapse.org/Synapse:syn60868042/wiki/628716.

Ethics Approval: "Not applicable."

Conflicts of Interest: The authors declare no conflicts of interest to report regarding the present study

References

1. Hasan AM, Al-Waely NKN, Ajobouri HK, Ibrahim RW, Jalab HA, Meziane F. A classification model of breast masses in DCE-MRI using kinetic curves features with quantum-Raina's polynomial based fusion. Biomedical Signal Processing and Control. 2023;84.

2. Alrubaie HD, Aljobouri HK, Aljobawi ZJ. Efficient Feature Selection Using CNN, VGG16 and PCA for Breast Cancer Ultrasound Detection. Revue d'Intelligence Artificielle. 2023;37(5):1255-61.
3. Pang Z, Zhu D, Chen D, Li L, Shao Y. A computer-aided diagnosis system for dynamic contrast-enhanced MR images based on level set segmentation and ReliefF feature selection. Comput Math Methods Med. 2015;2015:450531. Available from: https://www.ncbi.nlm.nih.gov/pubmed/25628755.
4. Narimani S, Roth Hoff S, Daehli Kurz K, Gjesdal KI, Geisler J, Grovik E. Comparative analysis of deep learning architectures for breast region segmentation with a novel breast boundary proposal. Sci Rep. 2025;15(1):8806. Available from: https://www.ncbi.nlm.nih.gov/pubmed/40087354.
5. Liao GJ, Henze Bancroft LC, Strigel RM, Chitalia RD, Kontos D, Moy L, et al. Background parenchymal enhancement on breast MRI: A comprehensive review. J Magn Reson Imaging. 2020;51(1):43-61. Available from: https://www.ncbi.nlm.nih.gov/pubmed/31004391.
6. Hasan AM, Al-Waely NKN, Aljobouri HK, Jalab HA, Ibrahim RW, Meziane F. Discrimination of invasive ductal and lobular carcinoma of the breast based on the combination of enhanced Legendre polynomial, kinetic features and deep learning features. Biomedical Signal Processing and Control. 2025;104.
7. Hasan AM, Aljobouri HK, Al-Waely NKN, Ibrahim RW, Jalab HA, Meziane F. Diagnosis of breast cancer based on hybrid features extraction in dynamic contrast enhanced magnetic resonance imaging. Neural Computing and Applications. 2023;35(31):23199-212.
8. M Hasan A, Khalaf M, M Sabbar B, W Ibrahim R, A Jalab H, Meziane F. Lung CT Image Segmentation Using VGG-16 Network with Image Enhancement Based on Bounded Turning Mittag-Leffler Function. Baghdad Science Journal. 2024;21(12):3892-902.
9. A Jalab H, W Ibrahim R, M Hasan A, Khalid Karim F, R Al-Shamasneh A, Baleanu D. A New Medical Image Enhancement Algorithm Based on Fractional Calculus. Computers, Materials Continua. 2021;68(2):1467-83.
10. Fridman N, Solway B, Fridman T, Barnea I, Goldstein A. BreastDCEDL: A standardized deep learning-ready breast DCE-MRI dataset of 2,070 patients. Sci Data. 2026;13(1):264. Available from: https://www.ncbi.nlm.nih.gov/pubmed/41540040.
11. Rehman NU, Wang J, Weiyan H, Ali I, Akbar A, Assam M, et al. Edge of discovery: Enhancing breast tumor MRI analysis with boundary-driven deep learning. Biomedical Signal Processing and Control. 2024;95.
12. Karimi D, Warfield SK, Gholipour A. Transfer learning in medical image segmentation: New insights from analysis of the dynamics of model parameters and learned representations. Artif Intell Med. 2021;116:102078. Available from: https://www.ncbi.nlm.nih.gov/pubmed/34020754.
13. Feng B, Zhou H, Feng J, Chen Y, Liu Y, Yu T, et al. Active contour model of breast cancer DCE-MRI segmentation with an extreme learning machine and a fuzzy C-means cluster. IET Image Processing. 2022;16(11):2947-58.
14. Khaled R, Vidal J, Vilanova JC, Marti R. A U-Net Ensemble for breast lesion segmentation in DCE MRI. Comput Biol Med. 2022;140:105093. Available from: https://www.ncbi.nlm.nih.gov/pubmed/34883343.
15. Douglas L, Bhattacharjee R, Fuhrman J, Drukker K, Hu Q, Edwards A, et al. U-Net breast lesion segmentations for breast dynamic contrast-enhanced magnetic resonance imaging. J Med Imaging (Bellingham). 2023;10(6):064502. Available from: https://www.ncbi.nlm.nih.gov/pubmed/37990686.
16. Hizukuri A, Nakayama R, Goto M, Sakai K. Computerized Segmentation Method for Nonmasses on Breast DCE-MRI Images Using ResUNet++ with Slice Sequence Learning and Cross-Phase Convolution. J Imaging Inform Med. 2024;37(4):1567-78. Available from: https://www.ncbi.nlm.nih.gov/pubmed/38441702.
17. Sahaya Pushpa Sarmila Star C, Inbamalar TM, Milton A. Automatic semantic segmentation of breast cancer in DCE-MRI using DeepLabV3+ with modified ResNet50. Biomedical Signal Processing and Control. 2025;99.
18. Garrucho L, Kushibar K, Reidel CA, Joshi S, Osuala R, Tsirikoglou A, et al. A large-scale multicenter breast cancer DCE-MRI benchmark dataset with expert segmentations. Sci Data. 2025;12(1):453. Available from: https://www.ncbi.nlm.nih.gov/pubmed/40108146.

19. Granzier RWY, Verbakel NMH, Ibrahim A, van Timmeren JE, van Nijnatten TJA, Leijenaar RTH, et al. MRI-based radiomics in breast cancer: feature robustness with respect to inter-observer segmentation variability. Sci Rep. 2020;10(1):14163. Available from: https://www.ncbi.nlm.nih.gov/pubmed/32843663.
20. Ali FI, AlJobouri HK, Hasan AM. Advancements in Cancer Detection: An Artificial Intelligence-Based Approach Using PET/CT Datasets. Al-Nahrain Journal for Engineering Sciences. 2025;28(3):451-60.
21. Petráš I. Novel Low-Pass Two-Dimensional Mittag–Leffler Filter and Its Application in Image Processing. Fractal and Fractional. 2023;7(12).
22. Huang G, Qin Hy, Chen Q, Shi Z, Jiang S, Huang C. Research on Application of Fractional Calculus Operator in Image Underlying Processing. Fractal and Fractional. 2024;8(1).
23. Yu F, Koltun V. Multi-scale context aggregation by dilated convolutions. arXiv preprint arXiv:151107122. 2015.
24. Ronneberger O FP, T B. U-Net: Convolutional Networks for Biomedical Image Segmentation. In: International Conference on Medical image computing and computer-assisted intervention. Springer; 2015. p. 234-41.
25. Liu T, Hu Y, Liu Z, Jiang Z, Ling X, Zhu X, et al. Deep Learning-Based DCE-MRI Automatic Segmentation in Predicting Lesion Nature in BI-RADS Category 4. J Imaging Inform Med. 2025;38(4):2053-62. Available from: https://www.ncbi.nlm.nih.gov/pubmed/39586911.
26. Li W, Newitt DC, Gibbs J, Wilmes LJ, Jones EF, Arasu VA, et al.. I-SPY 2 Breast Dynamic Contrast Enhanced MRI Trial (ISPY2). The Cancer Imaging Archive; 2022. Dataset. Data set.
27. Garrucho L, Kushibar K, Reidel CA, Joshi S, Osuala R, Tsirikoglou A, et al.. MAMA-MIA: A large-scale multicenter breast cancer DCE-MRI benchmark dataset with expert segmentations. Synapse; 2025. Dataset. Available from: https://www.synapse.org/Synapse:syn60868042/wiki/628716.
28. Ibrahim RW, Jalab HA, Karim FK, Alabdulkreem E, Ayub MN. A medical image enhancement based on generalized class of fractional partial differential equations. Quant Imaging Med Surg. 2022;12(1):172-83. Available from: https://www.ncbi.nlm.nih.gov/pubmed/34993069.
29. Khan MF, Khan S, Hussain S, Darus M, Matarneh K. Certain New Class of Analytic Functions Defined by Using a Fractional Derivative and Mittag-Leffler Functions. Axioms. 2022;11(11).
30. Mainardi F. Why the Mittag-Leffler Function Can Be Considered the Queen Function of the Fractional Calculus? Entropy (Basel). 2020;22(12). Available from: https://www.ncbi.nlm.nih.gov/pubmed/33266284.
31. Taha AA, Hanbury A. Metrics for evaluating 3D medical image segmentation: analysis, selection, and tool. BMC Med Imaging. 2015;15:29. Available from: https://www.ncbi.nlm.nih.gov/pubmed/26263899.
32. Muller D, Soto-Rey I, Kramer F. Towards a guideline for evaluation metrics in medical image segmentation. BMC Res Notes. 2022;15(1):210. Available from: https://www.ncbi.nlm.nih.gov/pubmed/35725483.